#### MODELING THE SPATIAL AND TEMPORAL EVOLUTION OF FRACTURED

### SYSTEMS WITH HETEROGENOUS MINERALOGY

- Parisa Asadi<sup>1,2</sup>, Md Fahim Salek<sup>1</sup>, Lauren E. Beckingham<sup>1\*</sup>
- 4 1 Department of Civil & Environmental Engineering, Auburn University, Auburn, AL, 36830,
- 5 USA
- 6 2 Carl ZEISS Microscopy innovation center, Dublin, CA, 94568, USA
- 7 \*leb@auburn.edu

#### **Abstract**

Reactive transport modeling is a critical tool for elucidating the coupling between geochemical reactions, transport processes, and fracture permeability. This study explores the implications of preferential clay-rich regions near fracture surfaces of a Mancos shale sample on the reactive evolution of the fracture using reactive transport simulations. These simulations utilized heterogenous mineralogy data obtained from an in-depth analysis of a clay-rich region near the fracture surface, sourced from a mechanically induced fracture. We compared these simulations with counterparts assuming homogeneous mineral distributions based on bulk X-ray diffraction (XRD) data and prior imaging of the sample matrix. The results consistently show increased reactivity in cells near the inlet and fracture surface across all scenarios. The most significant changes in porosity, mineral composition, and ion concentration occur in cells adjacent to the fracture at the system inlet. Comparative analysis reveals variations in mineral and porosity evolution among the three systems. Over longer simulation periods, dissolution and porosity increase occurs more rapidly in simulations reflecting mineral heterogeneity, particularly within the clay-rich region near the fracture. A sensitivity analysis of mineral surface area (SA) values

shows consistent trends using both low and high BET SA values over short timescales (days) but substantial disparities over longer timescales (years). These findings hold promise for improving our ability to predict the evolution of reactive fractures, with implications for subsurface CO<sub>2</sub> sequestration and oil recovery. In summary, this study advances our understanding of reactive transport in fractured systems, offering new avenues for predictive modeling.

- 30 Keywords: Reactive fracture evolution, Mineral dissolution rates, Heterogeneous mineralogy,
- 31 Clay-rich regions, Porosity evolution, Surface area variations.

#### 1. Introduction

The global temperature has increased due to CO<sub>2</sub> emissions from human activities. Geologic CO<sub>2</sub> sequestration offers an efficient and sustainable solution for reducing atmospheric CO<sub>2</sub> levels. The rapid development of subsurface organic-rich shales for hydrocarbon recovery in past years has opened up the possibility of utilizing these hydraulically fractured shale reservoirs as potential target reservoirs for CO<sub>2</sub> sequestration. Shales have a low permeability and high sealing capacity which make them potential candidates for CO<sub>2</sub> sequestration given porosity is increased by artificial fracturing. With the right reservoir conditions, injection of CO<sub>2</sub> into shale reservoirs can result in incremental oil recovery and permanent storage of CO<sub>2</sub> in geological formations. <sup>1</sup> Shales are also important caprock formations for sequestration in underlying saline aquifers where caprock fractures may pose a risk to the permanence of storage. To evaluate the CO<sub>2</sub> sequestration potential and security of these fractured networks, we need to better understand the geochemical reactions at CO<sub>2</sub>-fluid-shale interfaces and how they affect the flow and CO<sub>2</sub> storage permanence.

In these fractured heterogenous networks, fractures apertures can be impacted by geochemical reactions including mineral dissolution and precipitation. As CO<sub>2</sub> dissolves into formation brine, the pH of the system is lowered. Resulting acidic conditions may favor dissolution of primary minerals. <sup>2–10</sup> Dissolution of carbonate minerals, such as calcite or dolomite, can buffer the pH. As minerals dissolve, ions are released into solution such that conditions favoring precipitation of secondary minerals may develop. These mineral reactions may occur on fracture surfaces or in the low permeability matrix adjacent to fractures and will impact fracture permeability. <sup>7–9, 11–12</sup>

Previous research studies showed rock composition plays a critical role in fracture development. <sup>13–18</sup> Brittle minerals, such as silica, feldspars, and carbonates, tend to produce many highly conductive fractures under stress<sup>15, 19</sup>, whereas ductile minerals, such as organic matter or clays, are more prone to form microfractures. <sup>20,21</sup> These observations show the importance of mineral components in fracture formation.

Reactive transport modeling is an essential tool to simulate complex geochemical reactions in porous media that can impact formation properties. To date, most of the reactive transport modeling research on heterogeneous shale formations have focused on mechanical properties. Few studies have considered relationships between fracture surface mineralogy and the fracture evolution or propagation 15,17,20,22 with most simulations simplified by considering bulk formation mineralogy data obtained from XRD information. However, this may not accurately reflect the reactive minerals as bulk mineralogy does not consider mineral distribution, which may result in simulations unable to accurately reflect actual mineral reactions that will occur. Physical heterogeneity, such as heterogeneity in fracture permeability, is also controlled by the spatial

variation of mineralogy<sup>11</sup> which is not reflected in simulations using homogenous mineralogy distributions based on bulk sample analyses.

Mineral distribution also has an important role in controlling fracture formation. Several studies 15,17,20,23,24 have noted a relationship between individual mineral grains and the locations where fractures form, mostly focusing on the general mineral sealing capabilities or composition in which fractures tend to form. The distribution of mineral phases, particularly those that are highly reactive, is also anticipated to play an important role in controlling mineral reactions on fracture surface and the associated evolution of the fracture. 25,26 Literature considering reactions in porous media have additionally noted the importance of taking mineral heterogeneity into consideration 2,3,27–30, albeit not in fractured media. As mineral dissolution or precipitation reactions occur in fractured media, fracture aperture and permeability may be enhanced or reduced. 20 Evaluation of these highly heterogenous, complex systems, however, is challenging such that there is limited understanding and predictive capabilities to discern if reactions will lead to enhanced or reduced fracture flow. In addition, no study has particularly investigated the impact of varying multi-mineralogic fracture surface and matrix compositions on the reactive evolution of the fracture and surrounding matrix.

The objective of this work is to evaluate the impact of variations in mineralogy of the fracture surface and surrounding matrix on simulated mineral reactions and reaction rates between minerals and CO<sub>2</sub> saturated brine. It should be noted that a simplified model system is used here to consider implications of mineral heterogeneity on reactive fracture evolution while, macroscopic roughness<sup>11-15,18,22,24</sup> and multiphase flow<sup>62</sup> can further complicate mineral reactions and reactive fracture evolution. The mineral composition and distribution measured from image analyses of SEM-BSE images<sup>25</sup> are first used here to evaluate geochemical reactions and the

system evolution using reactive transport simulations. Simulations consider the extent of mineral reaction, reaction rates and fracture surface evolution in the context of geologic CO<sub>2</sub> storage at two timescales, a short (days) time scale and a long (years) time scale that are pertinent for understanding reactions for typical laboratory experiments and field conditions, respectively. Complementary simulations are then carried out using only the mineralogy of the matrix determined from analysis of SEM images<sup>25</sup> and bulk XRD analysis of the sample. Simulation results, including the evolution of mineral volume fractions, major ion concentrations, pH, porosity and mineral volume fraction and ion concentrations are then compared. The results obtained from this work will improve our ability to predict reactive fracture evolution and understand its implications for subsurface CO<sub>2</sub> sequestration and oil recovery.

# 2. Data and Methodology

### 2.1 Sample

In this work, observations of a Mancos shale sample from *Brunhoeber et. al.* (2021) <sup>25</sup> are used. This formation is stratigraphically located in the Mid-western United States. In *Brunhoeber et al.* (2021) <sup>25</sup>, Mancos shale core samples (Kocurek Industries Inc.) 1" by 2" were fractured by applying unconfined uniaxial compressive stress with 100kN load cell. To prepare the sample for imaging analysis, polished thin sections were created (Applied Petrographic Services Inc). Samples consisted both of section parallel and perpendicular to the fracture surface. 2D Scanning Electron Microscopy images were then collected of prepared thin sections using a Zeiss EVO 50 Variable Pressure Scanning Electron Microscope at Auburn University. The mineralogy, mineral abundances, and mineral volume fractions were determined from analysis of the 2D SEM images (Figure. 1 a, b). Readers are referred to Qin and Beckingham (2019)<sup>3</sup> if interested on accuracy of

mineral identification of the utilized SEM device in different resolutions. These data, as well as mineralogy obtained via powder XRD analysis of the bulk sample<sup>25</sup>, were used here and are reported in Table 1. Quantitative XRD analysis was performed on the Mancos samples using a Bruker D2 Phaser X-Ray Diffractometer. The XRD data were processed with DIFFRAC.EVA by Bruker using the Crystallography Open Database (COD) to identify the phases and estimate the weight percent of each mineral present using the Relative Intensity Ratio (RIR) method built into the software<sup>25</sup>. Mineral volume fractions are defined as mineral volume percentage within the porous medium (m³ mineral volume/m³ total porous medium volume).

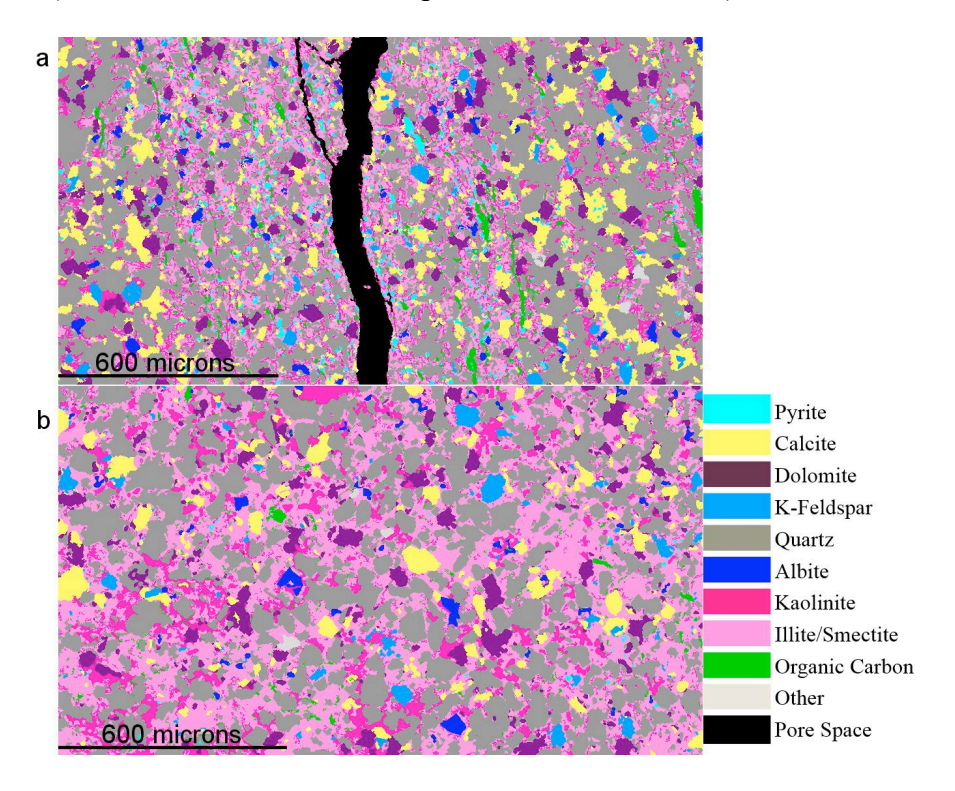


Figure 1. Processed SEM-EDS mineral maps of the near fracture matrix. (a) shows the matrix perpendicular to the imaged fracture surface, and (b) shows the matrix parallel to the fracture. Reproduced from Brunhoeber et al., Role of Mineralogy in Controlling Fracture Formation, ACS Earth Space Chemistry.<sup>25</sup> Copyright 2021. American Chemical Society.

Analysis of processed images (Figure. 1) in *Brunhoeber et. al.* (2021)<sup>25</sup> showed the presence of a clay rich region near the fracture surface and determined the fracture preferentially formed at kaolinite-kaolinite interfaces. Quantitative analysis of mineral distributions using a cross-correlation approach showed that clay minerals were 16.7 times more likely to be present than carbonate minerals near the fracture surface. <sup>25</sup> This clay rich region extended roughly 200 microns into the surrounding matrix, confirming preferential formation of the fracture within a defined clay-rich lithology.<sup>25</sup>

Table 1. Mineral volume fractions calculated from *Brunhoeber et. al.* (2021) <sup>25</sup>, specific surface area and rate constants for reactive transport simulations at reservoir condition as obtained from the literature for muscovite obtained from Oelkers et al. (2008) <sup>31</sup>, kaolinite obtained from Carroll and Walther (1990) <sup>32</sup> and Ganor et al. (1995)<sup>33</sup>, illite obtained from Gu and Evans (2007) <sup>34</sup>, K-Feldspar obtained from Bevan and Savage (1989) <sup>35</sup>, albite obtained from Chen and Brantley (1997) <sup>36</sup>, quartz obtained from Knauss and Wolery (1988) <sup>37</sup> and Brady and Walther (1990 & 1989) <sup>38,39</sup>, pyrite and dolomite obtained from Palandri and Kharaka (2004) <sup>40</sup>, and calcite obtained from Alkattan et al. (1998) <sup>41</sup>. The clay-rich region refers to the 200-micron region surrounding the fracture surface and the surrounding matrix is the matrix >200 microns from the fracture surface.

		Volume fraction (%)			Surface area		Rate constan t	
Minerals	Chemical Formula	XRD	Images of matrix paralle I to the fractur e	Images perpendicular to fracture		SSA low	SSA high	Log k
				Clay- rich region	Surroundin g matrix	BET (m²/g	BET(m²/g)	°C)
Muscovite	$KAl_2[AlSi_3O_{10}]$	6.8	-	-	-	1.10	3.40	-12.7
Kaolinite	$Al_2Si_2O_5(OH)_4$	3.0	9.7	60.6	8.9	3.17	19.50	-12.4
Illite	$K_{0.65}Al_{2.0}[Al_{0.65}Si_{3.35}O_{10}](OH)_2$	7.6	32.9	0.0	19.6	42.00	66.80	-13.4
K Feldspar	KAlSi <sub>3</sub> O <sub>8</sub>	6.3	1.9	1.6	1.7	0.11	1.52	-11.7
Albite	NaAlSi <sub>3</sub> O <sub>8</sub>	7.5	1.0	0.3	1.3	0.04	0.49	-11.1
Quartz	SiO <sub>2</sub>	49.0	36.3	14.9	46.5	0.02	0.11	-11.6

Pyrite	FeS <sub>2</sub>	0.1	0.1	1.2	2.3	0.03	2.80	-7.9
Calcite	CaCO₃	7.5	5.3	9.5	10.3	0.01	1.64	-4.2
Dolomite	CaMg(CO <sub>3</sub> ) <sub>2</sub>	6.2	5.7	1.9	6.0	0.06	0.07	-4.8

# 2.2 Reactive transport simulations

## 2.2.1 Model description

CrunchFlow<sup>42</sup> was used to build a reactive transport model coupling the solute transport, flow, and multiple species kinetic evolution for a CO<sub>2</sub>-saturated brine injection system with various defined mineralogy (Figure 2). CrunchFlow is a general-purpose continuum scale multicomponent reactive transport simulator that handles advective, diffusive, and dispersive transport and an arbitrary number of mixed equilibrium and kinetic reactions. The software is able to simulate single-phase flow in heterogeneous domains, including fracture flow<sup>43</sup>.

Here, two-dimensional transient reactive transport model systems were developed (Figure. 2). Models consisted of a matrix of 3 × 5 grid cells proceeded by a 'ghost' cell (treated as a boundary condition) containing a constant partial pressure of CO<sub>2</sub> in equilibrium with formation brine that acted as a constant source of CO<sub>2</sub>-saturated brine throughout the simulations. Cells were 3-millimeter long and 0.2-millimeter wide for both the fracture and clay-rich area (Figure. 2) and 1.8-millimeter width for the surrounding matrix cells.

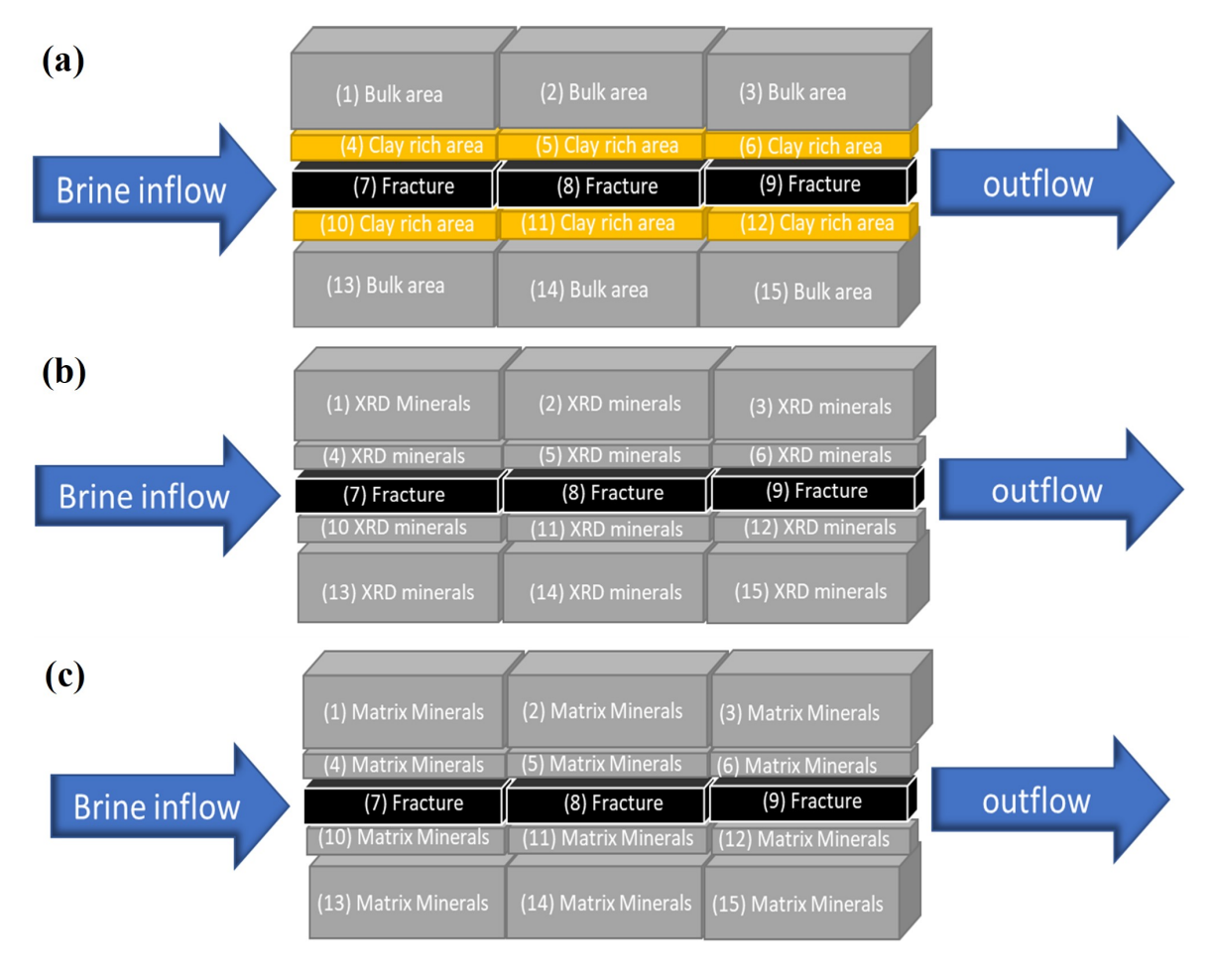


Figure 2. Diagram of the simulation system where a) corresponds to mineralogy determined from images perpendicular to the fracture (perpendicular-heterogeneous model), b) reflects mineralogy determined from bulk XRD analysis of the sample (XRD-homogeneous model), and c) captures mineralogy observed in images of the matrix in a sample parallel to the fracture (parallel-homogeneous model).

The mineral cells were initialized based on mineral volume fractions determined from imaging analysis of thin sections in Brunhoeber et. al. (2021) <sup>25</sup> and XRD information<sup>25,44</sup>, given in Table 1. Three model scenarios with varying mineralogy were considered. This included a simulation with heterogenous mineral distribution informed by images perpendicular to the fracture (perpendicular-heterogeneous model) which reflects the clay-rich near fracture region. Two additional models with homogenous distributions of mineralogy as given by bulk XRD

analysis (XRD-homogeneous model) and imaging of the matrix in a sample parallel to the fracture (parallel-homogeneous model) were also considered. For the heterogenous system (Figure 1a and Figure 2a), the mineral cells consist of clay-rich cells near the fracture (cells from 4 to 6 and 10 to 12) with 60.6% kaolinite, fracture cells (cells from 7 to 9) with 0.2-millimeter width and surrounding matrix cells with 46.5% quartz (cells from 1 to 3 and 13 to 15). This scenario is representative of the real, observed and quantified mineral distributions around the fracture in contrast to the other scenarios that use the bulk mineralogy. For the homogenous scenarios, all mineral cells have the same composition initialized either using mineral volume fractions determined from the XRD analysis or images of the matrix in samples parallel to the fracture (Table 1). The XRD volume fractions consist predominantly of quartz (49.0%) with ~15% feldspar minerals and relatively equal amounts (6-7%) of muscovite, illite, calcite, and dolomite while the mineral composition of the matrix determined from the image mainly consists of quartz (36.3%) and illite (32.9%). The complete mineralogy of each system is in Table 1. The chemical formula of illite (K<sub>0.65</sub>Al<sub>2.0</sub>[Al<sub>0.65</sub>Sl<sub>3.35</sub>O<sub>10</sub>](OH)<sub>2</sub>) was determined from SEM EDS analyses.

While this study used a simplified fracture geometry in the modeling, it should be noted that the images used to construct the fractured model (the perpendicular-heterogeneous model) are the actual, rough fracture surfaces. As such, the model captured the real variations in mineral accessibility on a rough fracture surface and as a result, the variations in the surface area of the minerals were considered in these simulations.

In the simulations, CO<sub>2</sub> acidified brine enters the domain starting from a time of 0 hours. Simulations track the evolution of the formation mineralogy, including volume fractions and porosity, as well as the composition of the brine. The corresponding estimated temperature and pressure at the sample depth, 1066 m, is 50 °C and 100 bar, calculated based on a temperature

gradient of 25 °C/km and surface temperature of 25 °C and pressure gradient of 100 bar/km <sup>45,46</sup>. The upstream location refers to the first internal column of cells near the inlet, midstream the central internal column cells, and downstream the third column of cells, furthest from the source of injection. Here, a simplified model system is used to consider implications of mineral heterogeneity on reactive fracture evolution while, macroscopic roughness<sup>11-15,18,22,24</sup> and multiphase flow<sup>62</sup> can further complicate mineral reactions and reactive fracture evolution.

# 2.2.2 Brine chemistry, flow and boundary conditions

The initial formation brine chemistry (Table 2) was determined by simulating equilibrium between the XRD determined bulk mineralogy with 1 mol/kg NaCl brine in a closed batch system under 50° C for 10,000 years. The resulting initial pH, based on charge balance, was 8.34. This brine composition was used in subsequent flow through simulations for all three simulations.

Table 2. Simulated brine chemistry of the Mancos formation.

Ion	Concentration (mol/kg fluid)
CO <sub>2</sub> (aq)	1.14 x 10 <sup>-05</sup>
Ca <sup>++</sup>	4.12 x 10 <sup>-01</sup>
Mg <sup>++</sup>	1.71 x 10 <sup>-02</sup>
Fe <sup>++</sup>	4.51 x 10 <sup>-07</sup>
K <sup>+</sup>	3.25 x 10 <sup>-04</sup>
Al <sup>+++</sup>	3.39 x 10 <sup>-07</sup>
SiO <sub>2</sub> (aq)	2.33 x 10 <sup>-04</sup>
рН	8.34
Na <sup>+</sup>	1.41 x 10 <sup>-01</sup>

HS-	7.90 x 10 <sup>-07</sup>
Cl <sup>-</sup>	1.00
SO <sub>4</sub>	1.13 x 10 <sup>-07</sup>

In flow through simulations, CO<sub>2</sub> at a partial pressure of 100 bar was equilibrated with simulated formation brine in a 'ghost' boundary cell. Starting at a time of zero, the CO<sub>2</sub> saturated brine was flowed through the domain at a constant flowrate of 0.92 m/day <sup>47</sup> and the evolution of major ions and mineral volume fractions tracked. The solubility of CO<sub>2</sub> in the formation brine was calculated in CrunchFlow using the Duan and Sun model based on the formation temperature and pressure. <sup>48</sup> The corresponding conditions result in a CO<sub>2</sub> saturated brine with a pH of 2.99. Precipitation of potential secondary mineral phases was also considered where the potential precipitating phases were selected using the database sweep option in CrunchFlow. The tortuosity, permeability for mineral cells, and diffusion coefficient were 4.6 obtained from Hu et al. (2019) <sup>49</sup>, 5.92 x 10<sup>-20</sup> m<sup>2</sup> obtained from Hu et al. (2019) <sup>49</sup> and Backeberg et al. (2017) <sup>50</sup> and 10<sup>-14</sup> obtained from Du and Nojabaei (2020) <sup>8</sup> and Hu et al. (2019) <sup>49</sup>.

The width of the fracture (0.2 millimeter) and clay-rich area (0.2 millimeter) were obtained from the image (Figure. 1a) and the permeability for the fracture cells was estimated by the cubic law for fracture permeability <sup>9,51,53</sup>:

Fracture permeability = 
$$\frac{W_h^2}{12}$$
 (1)

where  $W_h$ , is the hydraulic aperture of the fracture, defined as the aperture of a smooth-walled conduit that has the same permeability as the real rough-walled fracture <sup>54,55</sup>. Fracture permeability is a function of the average opening (aperture) of the fracture and the roughness of the fracture faces that create tortuous flow paths for the fluids. <sup>51,52,54</sup>

In the simulations in which the porosity evolves due to geochemical reactions, the evolution of permeability is updated according to:

$$k = k_0 \frac{\phi^3}{\phi_0^3} \tag{2}$$

- where k is the permeability and  $k_0$  and  $\phi_0$  are the initial permeability and porosity, respectively.
- 231 2.2.3 Mineral specific surface areas and reaction rates
- Mineral specific surface areas measured using the BET method <sup>56</sup> in previous studies were collected from the literature and used here. For a given mineral phase, BET surface areas vary up
- 234 to 4 orders of magnitude <sup>20,57</sup> depending on sample source, sample condition, adsorption method
- used, etc. Here, the sensitivity of models to mineral surface areas (SA) was investigated using the
- 236 high and low BET values for SA from the literature and the resulting impact on mineral reaction
- and porosity evolution compared.

- 238 CrunchFlow uses parallel rate laws that can account for pH dependence to simulate mineral
- reactions as given by, Steefel et. al. (2015) 42

- Here,  $r_s$  corresponds to the reaction rate, the mineral reactive surface area is depicted as A, the
- equilibrium constant  $K_a$  for the 'a'th parallel reaction, and N is the number of parallel reactions.
- The exponent  $p_{ia}$  captures the dependence of a species i on the 'a'th parallel reaction,  $\prod_{i=1}^{N_c + N_x} a_i^{p_{ia}}$
- 244 explains the degree of equilibrium effect of ions in solution. Exponents n and M capture the
- 245 nonlinearity and are experimentally determined. The ratio of the equilibrium constant  $K_s$  and ion
- 246 activity product  $Q_s$  reflects the deviation of the system from equilibrium. Rate constants were
- obtained from prior experimental works in the literature, interpolated following the Beckingham

et al. (2016) <sup>30</sup> at anticipated formation conditions post CO<sub>2</sub> injection corresponding to a temperature of 50 °C and pH of 2.99. The simulated pH of the system was determined via charge balance.

#### 3. Results and discussion

- Here, the results for simulations with heterogenous and homogenous mineral distributions are presented and further compared. Simulations consider the evolution of mineral volume fractions, ion concentrations, pH, and porosity. Time starts from negative values, indicating the state of the system before CO<sub>2</sub> injection. At a time of 0 h, CO<sub>2</sub>-saturated brine enters the system. Six different simulation sets were carried out which use two different BET SA sets for each of the three different mineral volume fraction systems (Figure. 2). The simulated evolution of the system is consistent for both sides of the fracture and as such results are only shown for part of the simulation domain, the fracture cells and surrounding mineral cells from one side of the fracture (cells 1-9 in Figure 2).
- 3.1 Evolution of mineral volume fractions
  - Figure 3 shows the simulated spatial and temporal evolution of mineral volume fractions for the scenario with heterogenous mineralogy capturing the clay-rich region near the fracture surface. In this simulation, the initial mineral volume fraction information and their distribution around the fracture and in the matrix correspond to those in the processed SEM image showing the perpendicular to fracture region (Figure 1a and Figure 2a). At a time of 0 hours, CO<sub>2</sub> saturated brine enters the system and leads to overall dissolution of the two carbonate phases calcite and dolomite in addition to pyrite and kaolinite, while the other mineral phases remain relatively stable during the first 20 days (cells from 1 to 3 in Figure 3). The calcite volume fraction rapidly decreases

from around 10% to 0.13% in almost all cells whereas dolomite has a slower dissolution rate, and its evolution varies across the domain. Pyrite and kaolinite dissolution initiate after depletion of calcite and dolomite. It should be noted, however, that pyrite dissolution requires oxygen. Initial oxygen concentrations in subsurface formations are anticipated to be low. However, oxygen may be introduced as an impurity during CO<sub>2</sub> injection, and it is not well understood if this would be substantial enough to promote pyrite dissolution in these subsurface systems. In the simulation here, it is assumed sufficient oxygen exists to promote pyrite dissolution but additional efforts beyond the scope of this work are needed to thoroughly understand which, and when, conditions favor pyrite dissolution in subsurface systems.

In the up-stream cells (first column), calcite and dolomite rapidly dissolve and are close to depletion in less than a day, around 12 and 19 hours, respectively. Pyrite and kaolinite dissolution then begin and continue throughout the simulation. Quartz, K-feldspar, albite and illite are stable throughout the first few days. In the mid- and down- stream cells (i.e., second and third columns from left in Figure. 3), up-stream calcite dissolution initially results in slight calcite precipitation that later dissolves. Calcite completely dissolves in the mid and down-stream cells occurs at ~24 and 30 hours, respectively. At early time in mid- and down- stream cells, dolomite initially precipitates. However, following consumption of calcite, dolomite begins dissolving. The average dissolution rate of dolomite increases after complete dissolution of calcite in the system. In addition, kaolinite dissolves in these cells at the same rate as it is dissolving in the up-stream cells. Other minerals remain almost stable in the short term and only quartz precipitates with 0.1% mineral volume fraction. The results for cells 7 to 9, which are representative of the fracture, also show a small amount of quartz precipitation.

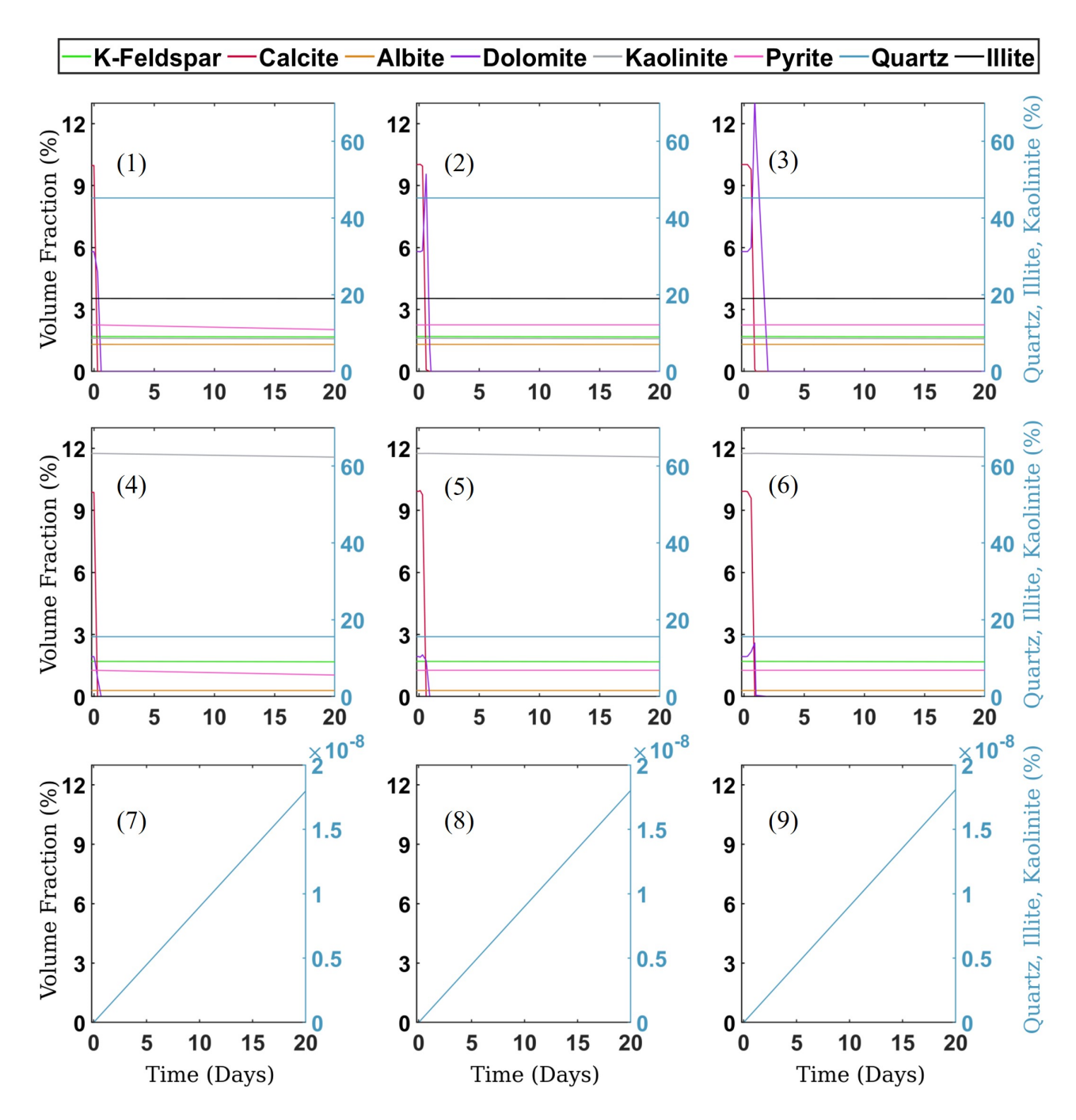


Figure 3. Simulated evolution of mineral volume fraction for the heterogenous mineralogy system defined using images perpendicular to the fracture (perpendicular-heterogeneous model) over the first 20 days of simulation for cells one to nine. Cells 1 to 3 are representative of the matrix, 4 to 6 the fracture surface, and 7 to 9 the fracture.

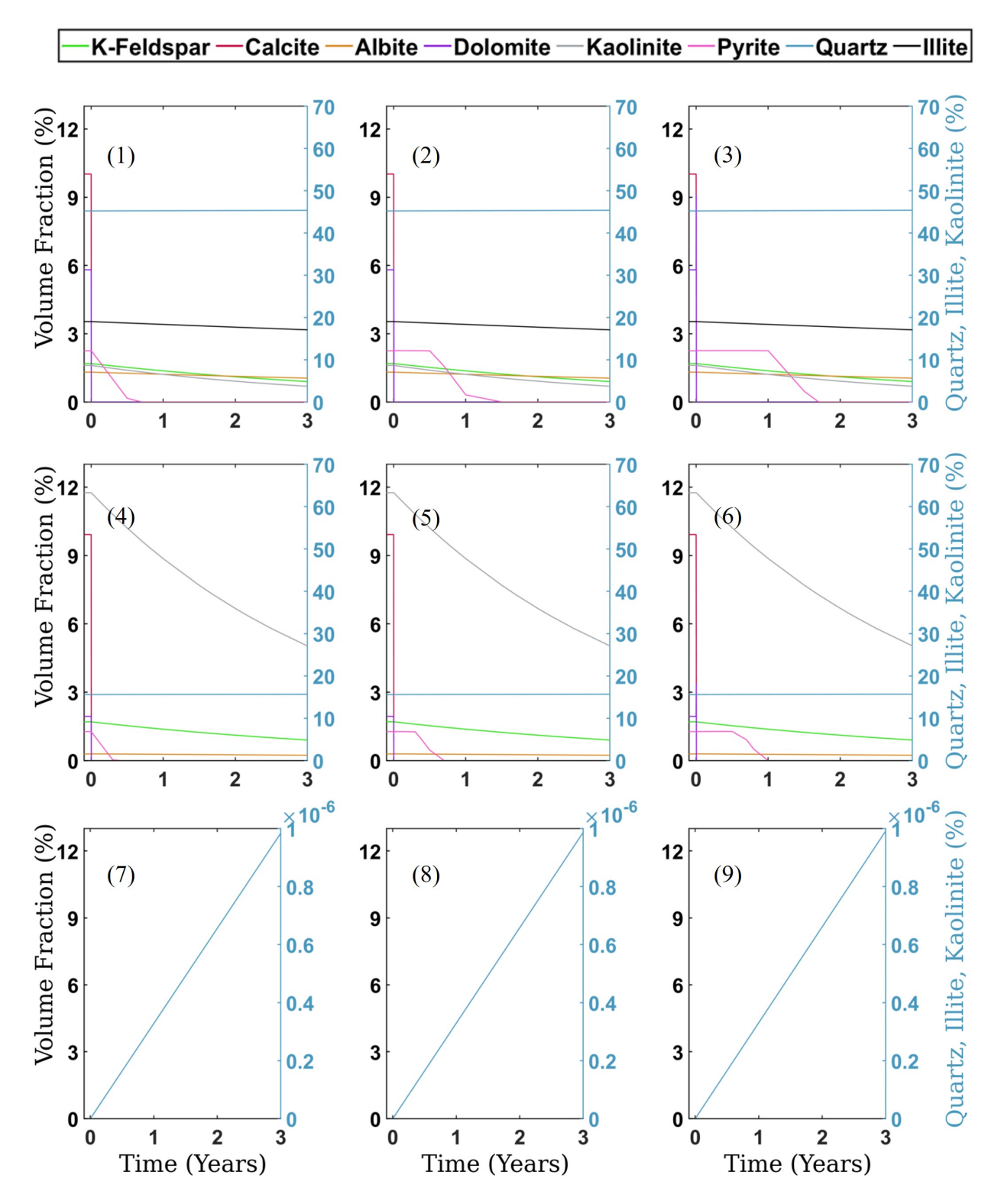


Figure 4. Simulated evolution of mineral volume fraction for systems with heterogenous mineralogy defined from the perpendicular images (perpendicular-heterogeneous model) for the first 3 years of simulation for cells one to nine. Cells 1 to 3 are representative of the matrix, 4 to 6 the fracture surface, and 7 to 9 the fracture.

The simulated evolution of formation minerals over 3 years is shown in Figure 4. Calcite and dolomite where are depleted in the first days of simulation, 0.5, 1.2, and 2 days for up-, midand down-stream cells, respectively. The average dissolution rate of kaolinite increases after almost complete dissolution of calcite in the system. Near the inlet (first column), pyrite initially remains stable then begins dissolving following almost complete dissolution of calcite in each cell. In mid- and down-stream cells, dissolution starts later due to some precipitation of pyrite coming from up-stream pyrite dissolution. Quartz is predicted to precipitate by 5% volume fraction over 3 years while K-feldspar dissolves by 1% volume fraction in the same period where its dissolution is slightly higher in cells adjacent to the fracture (i.e., cells from 4 to 6). Dissolution of albite and kaolinite is also investigated and indicate conditions favorable for dissolution of albite to small volume fractions (< 1 orders of magnitude of other minerals) whereas kaolinite dissolves up to 30% with smaller dissolution rates as time progresses. Changes in kaolinite are higher in cells adjacent to the fracture as is also true for K-feldspar.

The temporal and spatial mineral volume evolution for systems with homogenous mineralogy from XRD (XRD-homogeneous model) and parallel image analyses (parallel-homogeneous model) are presented in Supplementary Figures S1 to S4. As the CO<sub>2</sub>-saturated brine flows into both systems, dolomite and calcite rapidly dissolve in inlet mineral cells (first column), with the dolomite dissolution rate increasing after calcite depletion. In mid- and down- stream cells, dolomite first precipitates and then dissolves, which is similar to the heterogeneous scenario but with a lower amount of precipitation, to a volume fraction of 10% compared to 13% in the previous scenario. In general, for all scenarios, downstream calcite and dolomite dissolution is limited by increasing ion concentrations in solution from upstream calcite dissolution, resulting in non-uniform calcite volume fractions across the domain until all upstream calcite is consumed.

The rate of consumption, however, varies depending on the mineral distribution where simulations with uniform composition based on the XRD mineralogy (XRD-homogeneous model) have a higher calcite depletion rate followed by simulations accounting for the clay enriched near fracture region (perpendicular-heterogeneous model, Figure 2a) and, lastly, those of the image observed matrix (parallel-homogeneous model, Figure 2c).

Unlike dolomite and calcite, K-feldspar dissolution in homogenous scenarios occurs to a relatively uniform extent across the domain length as simulations progress, with a higher depletion rate for the XRD-homogenous scenario followed by simulations considering perpendicular-heterogenous and parallel-homogenous scenario informed by the image analysis. Pyrite and kaolinite also dissolve throughout the simulation domain in homogenous scenarios. While the dissolution rate of kaolinite is slower in these scenarios compared to the heterogenous system over the first 20 days, the dissolution rate of pyrite is higher here. Pyrite dissolution decreases from upstream to down-stream and as time progress in both homogenous systems. Considering real mineralogy and macroscopic fracture roughness resulted in more complex macroscopic fracture geometries and had some impact on mineral reaction rates. However, the overall observed trend in reactions, reaction rates, and implications of accounting for the heterogeneity in mineral geometry that were the focus of this work, was not largely impacted and the effect of roughness<sup>11-15,18,22,24,58-59</sup> and multiphase flow<sup>60-62</sup> and future investigation is required to understand the effect of these variables that is beyond the scope of this study.

Considering long-term simulations for the homogeneous systems (Supplementary Figures S2 and S4), calcite rapidly dissolves and is close to depletion around 0.5, 1 and 2 days in the upstream, mid-stream and down-stream cells for the XRD-homogeneous scenario. These values are 13 hours, 1 day, and 2 days and 3 hours, respectively, for the simulations using the homogeneous

bulk mineralogy from the image parallel to the fracture. The kaolinite dissolution rate, in these scenarios, is also slower than in the perpendicular-heterogenous scenario. Here, the kaolinite volume fraction reduces by 1.5% and 5% compared to a 30% reduction in the perpendicular-heterogenous scenario. The volume fraction of albite in simulations using the XRD mineralogy (XRD-homogeneous scenario) changes by 1.2% which is higher than the ones in both other scenarios. Muscovite is only present in the scenario using the XRD mineralogy and dissolves by 1.5% volume fraction. The volume fraction of K-feldspar decreases from 6% to 4% in the scenario using the XRD mineralogy which is 1% higher than in the other scenarios. In both homogeneous scenarios, quartz precipitates around 5%. In general, quartz does not vary across the simulation domain in all 3 scenarios and precipitates uniformly throughout the simulation domain throughout the duration of the simulations. Conversely, illite, K-feldspar, albite, and kaolinite dissolve and their dissolution varies across the simulation domain and from one scenario to the other.

### 3.2 Ion concentration and pH

The simulated evolution of major ion concentrations and pH in the CO<sub>2</sub>-brine system for heterogeneous system (perpendicular-heterogeneous scenario) is shown in Figure 5 over 20 days and Figure 6 for 3 years. As the simulation starts, the introduction of acidified brine with a pH of 2.995 at 0 hours results in a decrease in the pH in the mineral cell from the initial pH of 8.4 and increase in the concentration of calcium, magnesium and iron as calcite, dolomite, and pyrite dissolve (Figure 5 and 6) in up-, mid- and down-stream cells. Calcite dissolution rapidly buffers the pH to 4.4, 4.5, 4.5 in the up-stream, mid-stream and down-stream locations, respectively. The evolution of pH is closely coupled to decreasing calcite volume fraction. As calcite is consumed, the pH gradually drops to 2.99 reflecting a reduction in the extent of buffering. This occurs first in

cell closest to the inlet before propagating downstream. Magnesium ion concentration increases due to dolomite disillusion and decrease as time progress. Concentrations return to background levels as dolomite depletes after around 3 days. The increase in iron, aluminum and sulfate concentrations after calcite depletion reflect dissolution of illite, pyrite and kaolinite where concentrations are lowest in the grid cell closet to the inlet and increase with distance from the upstream or fracture cells. In the long-term, iron, aluminum and sulfate concentrations decrease after pyrite depletes, occurring faster in the grid cell closet to the inlet and decreasing with distance from the up-stream or fracture cells. No obvious change in aqueous silica or potassium concentrations occur within the simulation period.

The simulated major ion concentrations and pH evolution in the CO<sub>2</sub>-brine system for homogenous systems (XRD-homogenous and parallel-homogenous scenarios) are shown in Supplementary Figures S5 to S8 over 20 days and 3 years, respectively. Similar calcium, magnesium and pH evolution patterns are evident in these scenarios as explained for heterogeneous system (perpendicular- heterogeneous scenario), only occurring more rapidly as compared to the heterogenous system. In long-term simulations, the rate of decrease in iron, aluminum and sulfate concentrations after calcite depletion is faster (less than a year for these scenarios) in comparison with the simulations considering heterogenous mineral distributions that was a half year for inlet and near fracture cells and one and half year for other cells. This may be due to variations in mineralogy and different amounts of mineral volume fractions of illite, pyrite, muscovite and kaolinite. In addition, concentrations are lowest in the grid cell closet to the inlet and increase with distance from the up-stream or fracture cells.

Overall, the differences in pH and major ion concentrations between different cells are mostly temporal and observations from up-stream cells occurs in mid- and down-stream cells with

a  $\sim$ 2 day delay for calcium and magnesium in good agreement with the evolution of mineral volume fractions. Also, the concentrations are lowest in the grid cell closet to the inlet and increase with distance and time as minerals dissolve in  $CO_2$  acidic brine from the up-stream or fracture cells till the completed depletion of the mineral of interest. All patterns and orders follow those described for the different scenarios in the evolution of mineral volume fraction section.

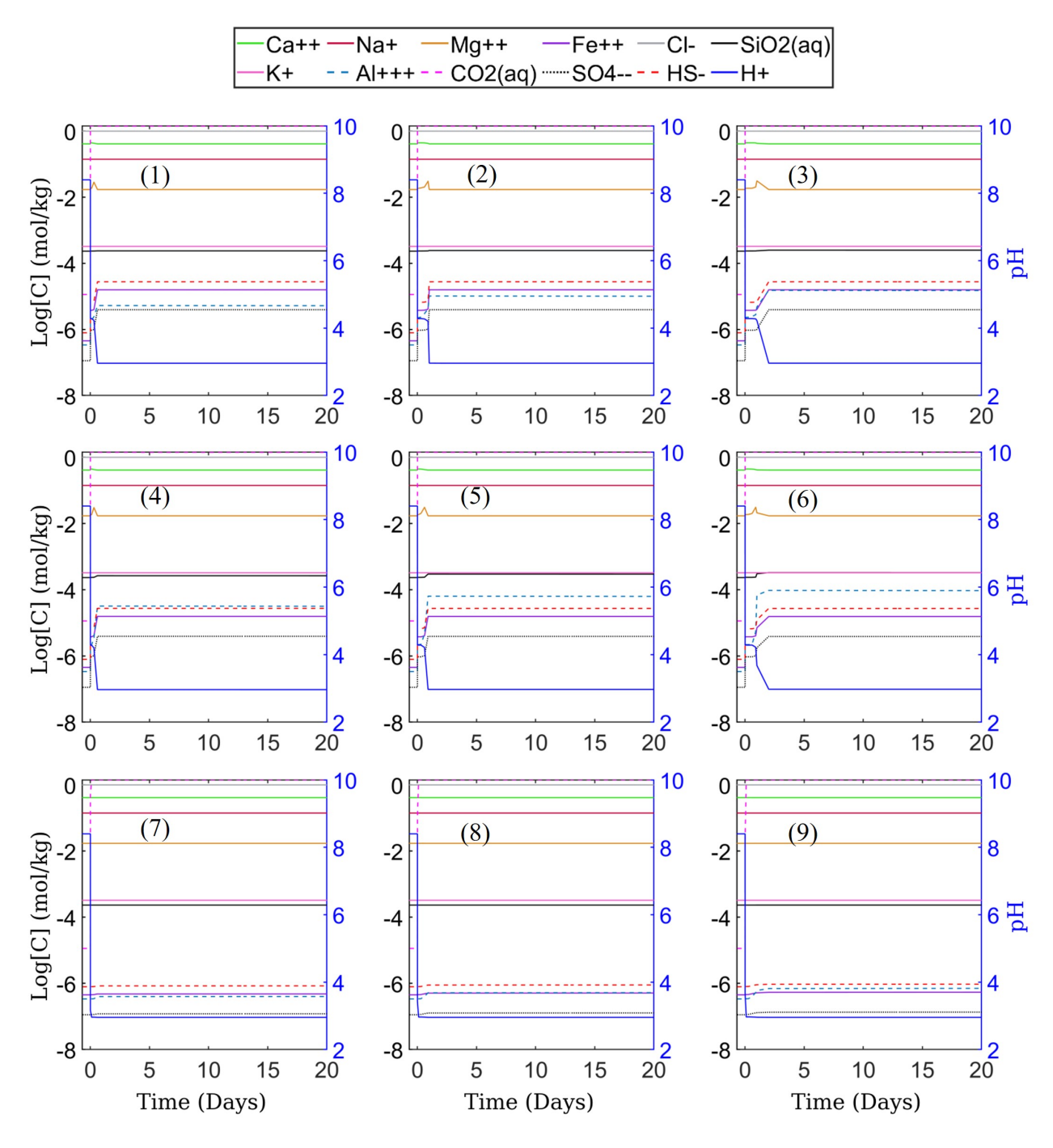


Figure 5. Simulated evolution of major ion concentrations and pH for the heterogenous mineralogy system (perpendicular-heterogeneous model) defined using images perpendicular to the fracture over the first 20 days of simulation for cells one to nine. Cells 1 to 6 are representative of the fracture surface and 7 to 9 are representative of the fracture.

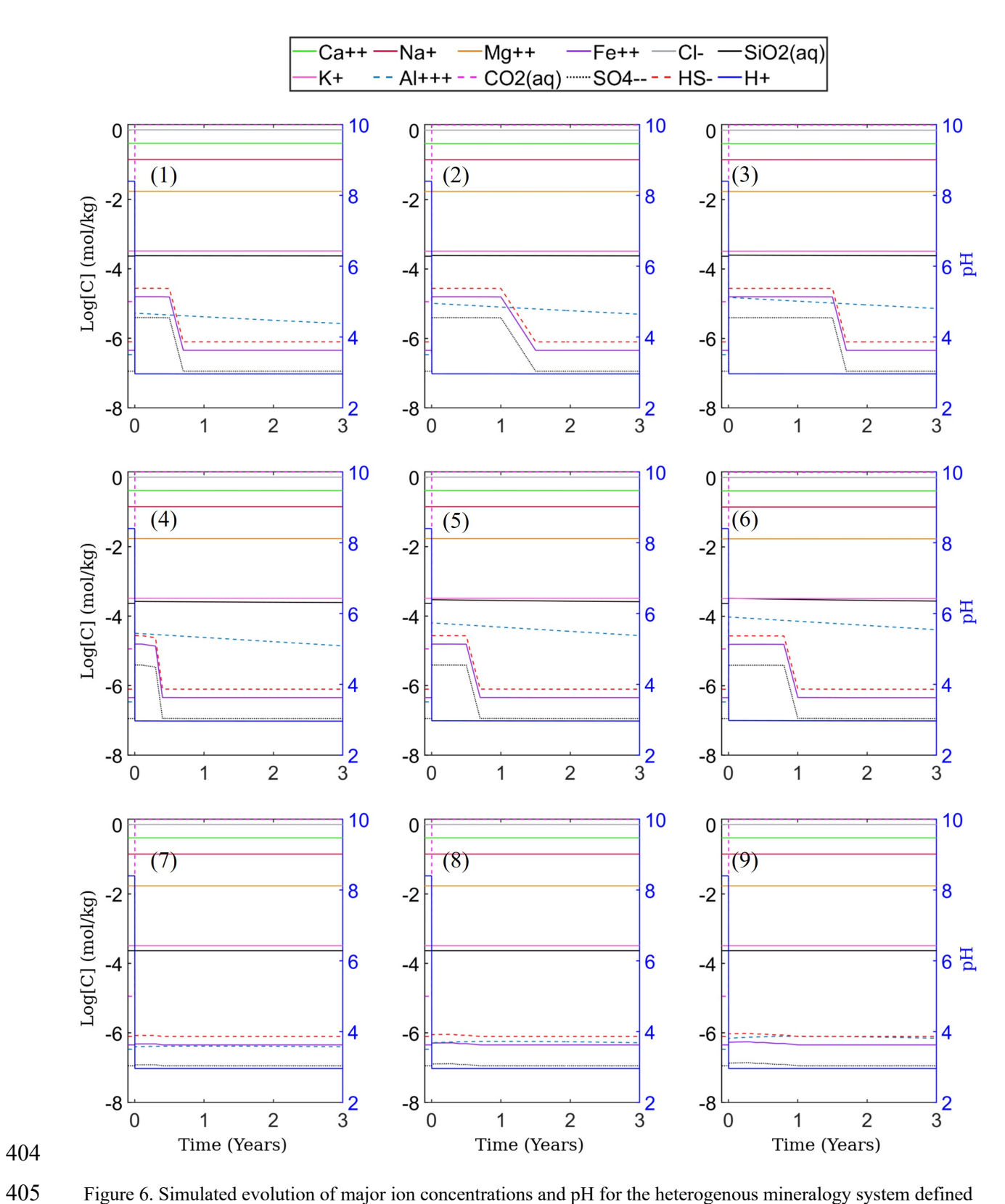


Figure 6. Simulated evolution of major ion concentrations and pH for the heterogenous mineralogy system defined

using images perpendicular to the fracture (perpendicular-heterogeneous model) depicting 3 years of simulation for cells one to nine. Cells 1 to 6 are representative of the fracture surface and 7 to 9 are representative of the fracture.

# 3.3 Porosity and overall Permeability Evolution

Simulated changes in porosity for the three different scenarios considering high and low BET SA over first 20 days and 3 years period are shown in Figure 7 and Figure 8, respectively. Changes in porosity reflect both mineral dissolution and precipitation reactions that occurr after introduction of CO<sub>2</sub>-acidified brine. In Crunchflow, the porosity (φ) is updated according to the evolving mineral volume fractions at each time step.

As shown in Figure 7, in the up-stream cell furthest from the fracture, porosity rapidly increases with a sharp slope until ~1 day following CO<sub>2</sub>-brine injection for all scenarios and continuous to gradually increase throughout the study duration. This is largely a result of dissolution of calcite and dolomite. After 20 days, the porosity in this cell is 22%, 20% and 17.5%, as compared to the initial value of 6% throughout the simulation for all scenarios with the largest increase in porosity for the perpendicular-heterogeneous model that reflects the clay-rich near fracture region and the smallest porosity increase for parallel-homogenous simulations using the bulk mineralogy from the imaging analysis of a parallel to fracture sample. This pattern and order are observed for mid- and down-stream cells furthest from the fracture (cells 1 to 3) due to similar mineralogy. However, the porosity increase is highest near the inlet and deceases away from the inlet largely due to variations in calcite dissolution.

For the first 20 days, there is little variation in simulated porosity with varied surface area for each scenario. The simulated evolution of porosity for cells closest to the fracture over 20 days shows porosity increases from 6% to 18.5%, 20% and 18% for the perpendicular-heterogeneous, XRD-homogenous, and parallel-homogenous scenarios, respectively. The change of the order may

be because of slower transport and reaction in the clay-rich region in the perpendicularheterogenous scenario compared to the XRD-homogenous scenario using the bulk XRD mineralogy.

Over longer time periods (Figure 8), porosity continues to increase with the expectation that the locations closest to the inlet and fracture have higher porosity. This is because downstream reactions are limited by elevated ion concentrations resulting from upstream dissolution. This also explains the lower porosity and slower depletion rates at the mid- and down-stream cells for perpendicular-heterogenous scenarios compared to the homogenous scenarios.

The reason behind the heightened impact of variations in BET surface area on porosity over extended timescales (Figure 8), as opposed to the short term, is attributed to the prevalence of kaolinite as a dominant reactive mineral. As illustrated in Table 1, the clay-rich area is comprised of 60.6% Kaolinite. While the high BET surface area (19.5 m²/g) is five times more than the low BET surface area (3.17 m²/g), the dissolution rate of kaolinite is slow. As such, substantial differences in the extent of reaction resulting from these differences in surface area are not evident over the 20 day simulation time frame and require longer simulation times to be realized.

The overall simulated change in porosity is different for each scenario, highlighting the importance of considering the clay-rich area next to the fracture that may cause up to a 20% difference in simulated porosity evolution. In addition, differences in the simulated porosity based on the selected surface area values are evident where higher surface area values result in larger simulated increases in porosity and permeability in these areas (based on equation 4.2). Extreme increases in porosity and permeability result in simulations using the high BET SA values for simulations that reflect the clay rich region near the fracture. It should be noted that with such large

increases, the fracture may no longer be stable and may collapse due to confining pressure. This, however, cannot be accounted for in the simulation approach considered here. Overall, simulations show fracture apertures slightly decrease due to a small amount of quartz precipitation throughout the simulation as the precipitation will increase the total mineral volume fraction in these cells and also slightly reduce the permeability in these areas.

The anticipated change in permeability can be estimated by the simulated evolution of porosity (Eqtn. 2). In the perpendicular-heterogeneous model, the simulated porosity increases from 6% to 22% after 20 days which corresponds to an estimated change in permeability from 5.92 x 10<sup>-20</sup> m<sup>2</sup> to 2.92 x 10<sup>-18</sup> m<sup>2</sup>. In the XRD-homogeneous model, the simulated porosity increases from 6% to 19% which corresponds to permeability increasing from 5.92 x 10<sup>-20</sup> m<sup>2</sup> to 1.88 x 10<sup>-18</sup> m<sup>2</sup>. In terms of the fracture permeability, substantial changes in aperture are not suggested by the simulation. Simulations suggest that fracture aperture will not be largely impacted in the simulated region of interest due to mineral dissolution and precipitation reactions. Overall, the results of this work suggest the importance of accurate accounting for mineral heterogeneity on simulated reactions and reaction rates. It should be noted that macroscale fracture roughness or multi-phase flow may further affect mineral reactions and reaction rates but are beyond the scope of this work.

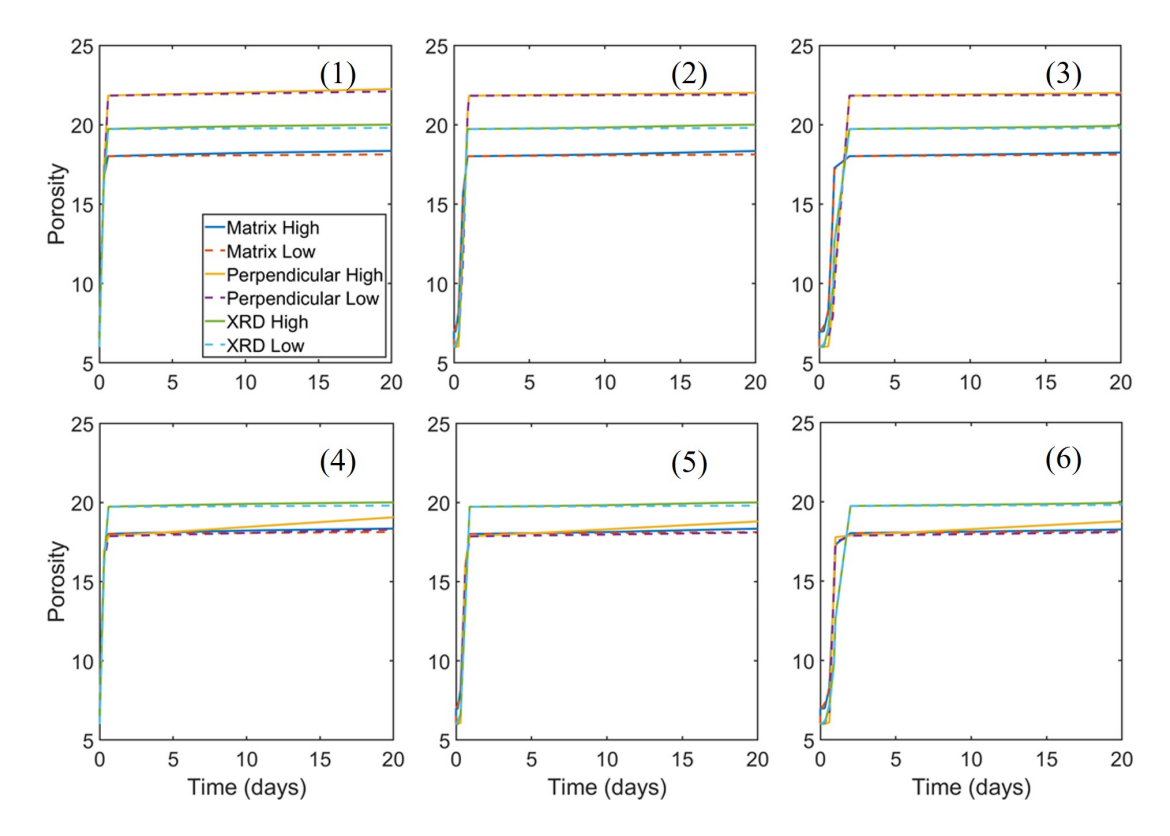


Figure 7. Simulated porosity (%) evolution over first 20 days in simulation cells 1 through 6 for different scenarios (Matrix High and Low: are results of parallel-homogenous models utilizing the matrix mineralogy obtained from images parallel to the fracture for high and low specific surface area, respectively; Perpendicular High and Low: are results of perpendicular-heterogenous models utilizing the mineralogy obtained from images perpendicular to the fracture for high and low specific surface area, respectively; XRD High and Low: are results of XRD-homogenous models utilizing the bulk mineralogy obtained XRD test result for high and low specific surface area, respectively)

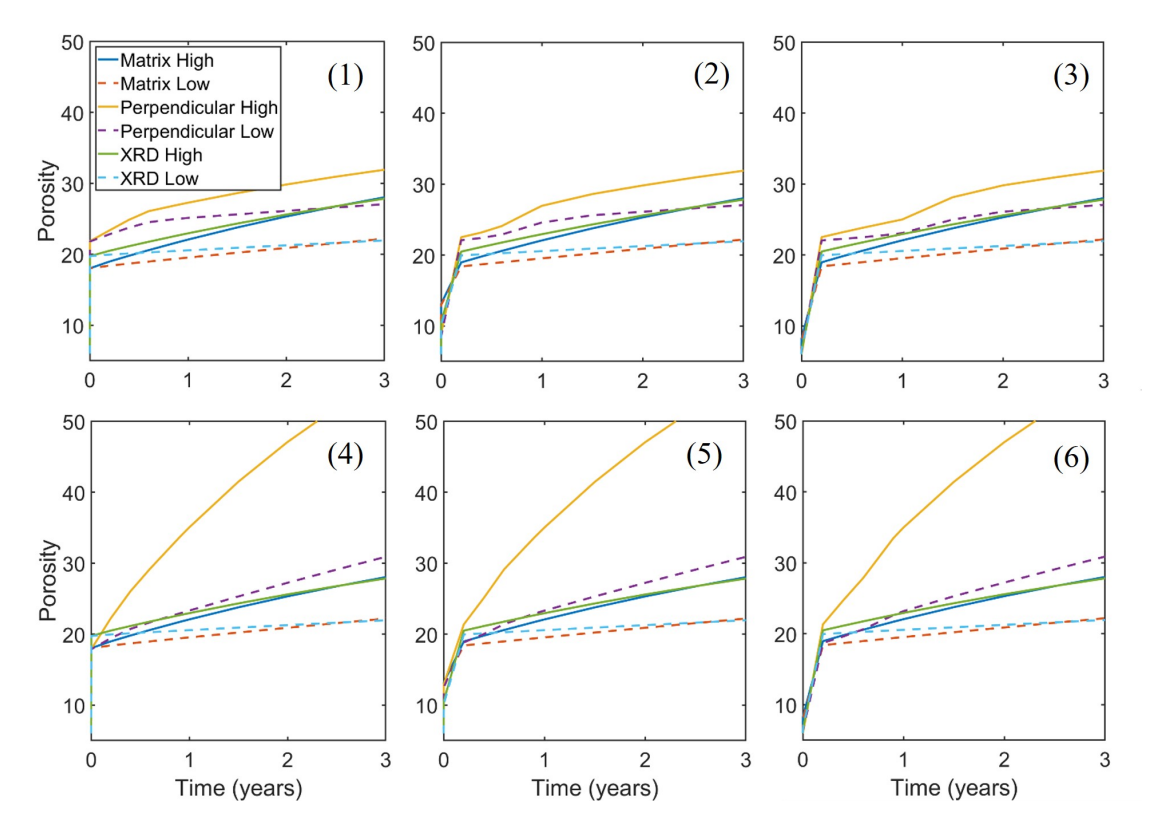


Figure 8. Simulated porosity (%) evolution over 3 years in simulation cells 1 through 6 for different scenarios (Matrix High and Low: are results of parallel-homogenous models utilizing the matrix mineralogy obtained from images parallel to the fracture for high and low specific surface area, respectively; Perpendicular High and Low: are results of perpendicular-heterogenous models utilizing the mineralogy obtained from images perpendicular to the fracture for high and low specific surface area, respectively; XRD High and Low: are results of XRD-homogenous models utilizing the bulk mineralogy obtained XRD test result for high and low specific surface area, respectively)

### 4. Conclusion

This study aimed to evaluate the impact of mineralogical variations on simulated mineral reactions and reaction rates in CO<sub>2</sub>-saturated brine on fracture surfaces and the surrounding matrix. The analysis focused on quantifying changes in porosity, mineral composition, and ion concentrations under various mineral distribution scenarios, with a particular emphasis on geologic CO<sub>2</sub> storage over both short and long timescales.

The findings unveil distinct temporal and spatial patterns in simulation outcomes, with cells situated near the inlet or fracture exhibiting more pronounced reactions, particularly in the upstream cells closest to the fracture surface. Similarities in the dissolution of calcite and dolomite are evident, albeit with different rates and extents of reaction. Furthermore, the dissolution of specific minerals in inlet cells has a cascading effect, leading to decelerated reactions and shifts in mineralogy in mid- and downstream cells, primarily due to diffusion dynamics.

The dissolution rates of minerals vary with mineral distribution scenario. Simulations informed by XRD data (XRD-homogenous models) have the highest calcite depletion rate, followed by perpendicular-heterogenous simulations considering the clay-rich region near the fracture and those utilizing parallel-homogeneous mineralogy from images. XRD-homogenous simulations exhibited a 20% faster calcite depletion rate compared to perpendicular-heterogenous simulations. K-feldspar dissolution also exhibits higher depletion rates in XRD-homogenous scenarios, followed by perpendicular-heterogeneous and parallel-homogeneous image-based scenarios. Substantial variations in the dissolution of minerals such as kaolinite, albite, and illite are evident with the most significant reduction in illite and kaolinite volume fractions in the perpendicular-heterogeneous scenario. Uniform quartz precipitation, and an associated slight decrease in fracture aperture, is observed in all scenarios.

Surface area variations play a pivotal role in shaping mineralogy and porosity, primarily during short-term simulations (first 20 days), where calcite and dolomite dissolution predominantly influenced porosity changes. The most rapid porosity increase, up to 22%, occurs in perpendicular-heterogeneous simulations representing the clay-rich region near the fracture, followed by 19% porosity increase for homogeneous simulations utilizing XRD mineralogy. In cells closest to the fracture, the highest porosity increase occurs in XRD-homogeneous

simulations, followed by perpendicular-heterogeneous simulations. Notably, surface area variations have minimal impact on porosity evolution in the long term (3 years).

Over long-time scales, mineral dissolution and porosity increase occurs more rapidly in perpendicular-heterogeneous mineralogy simulations (mimicking the clay-rich region), followed by XRD-homogeneous simulations. Unlike short-term simulations, variations in porosity significantly influence porosity evolution over time. Higher surface areas resulted in increased reaction rates and enhanced porosity development (up to a 12% more porosity evolution in perpendicular-heterogeneous compared to XRD-homogeneous simulations).

Different dissolution patterns are evident for various minerals across scenarios, impacting the simulated evolution of matrix porosity. As such, neglecting mineral distribution heterogeneity in simulations, especially in cells adjacent to the fracture, may lead to inaccuracies when representing mineral reactions. Here, these differences led to a difference in the simulated evolution of porosity in the matrix of 12%. Accurate accounting for mineral heterogeneity is critical when assessing fracture sealing potential under compressive stress, as larger reaction extents near the fracture surface and corresponding porosity increases may promote sealing, while less reactive regions near the fracture may retain permeability. These findings significantly enhance the ability to predict reactive fracture evolution and its implications for subsurface CO2 sequestration and oil recovery.

#### **Supporting Information**

The temporal and spatial mineral volume evolution for systems with homogenous mineralogy from XRD and parallel image analyses (Figures S1 to S4) and list of the chemical reaction equations for all minerals considered in the simulations within the fractured system (Table S1) are presented in Supplementary (PDF).

# 536 537 **Author information** 538 Corresponding Author Lauren E. Beckingham – Department of Civil and Environmental 539 Engineering, Auburn University, Auburn, Alabama 36830, United States; orcid.org/0000-0002-540 8433-9532; Email: leb@auburn.edu 541 Authors 542 Parisa Asadi – Carl ZEISS Microscopy innovation center, Dublin, CA, 94568, United States, 543 and Department of Civil and Environmental Engineering, Auburn University, Auburn, 544 Alabama 36830, United States Md. Fahim Salek - Department of Civil and Environmental Engineering, Auburn 545 546 University, Auburn, Alabama 36830, United States 547 **Notes** 548 The authors declare no competing financial interest. 549 Acknowledgements 550 Acknowledgment is made to the Donors of the American Chemical Society Petroleum Research 551 Fund and the National Science Foundation (Grant No: 1847243) for support of this research. 552 553 Reference

- 554 1. Kumar, N., Sampaio, M. A., Ojha, K., Hoteit, H., & Mandal, A. (2022). Fundamental aspects, mechanisms
- and emerging possibilities of CO<sub>2</sub> miscible flooding in enhanced oil recovery: A review. Fuel, 330, 125633.
- 556 2. Beckingham, L. E., Steefel, C. I., Swift, A. M., Voltolini, M., Yang, L., Anovitz, L. M., ... & Xue, Z. (2017).
- 557 Evaluation of accessible mineral surface areas for improved prediction of mineral reaction rates in porous
- media. Geochimica et Cosmochimica Acta, 205, 31-49.
- 3. Qin, F., & Beckingham, L. E. (2019). Impact of image resolution on quantification of mineral abundances
- and accessible surface areas. Chemical Geology, 523, 31-41.

- 561 4. Iloejesi, C. O., & Beckingham, L. E. (2021b). Influence of storage period on the geochemical evolution of a
- compressed energy storage system. Frontiers in Water, 100.
- 563 5. Iloejesi, C. O., & Beckingham, L. E. (2021). Influence of storage period on the geochemical evolution of a
- 564 compressed energy storage system. Frontiers in Water, 3,100-113.
- 565 6. Wu, S., Zou, C., Ma, D., Zhai, X., Yu, H., & Yu, Z. (2019). Reservoir property changes during CO2-brine
- flow-through experiments in tight sandstone: Implications for CO2 enhanced oil recovery in the Triassic Chang 7
- Member tight sandstone, Ordos Basin, China. Journal of Asian Earth Sciences, 179, 200-210.
- 568 7. Steel, L., Liu, Q., Mackay, E., & Maroto-Valer, M. M. (2016). CO2 solubility measurements in brine under
- reservoir conditions: A comparison of experimental and geochemical modeling methods. Greenhouse Gases: Science
- 570 and Technology, 6(2), 197-217.
- 571 8. Du, F., & Nojabaei, B. (2020). Estimating diffusion coefficients of shale oil, gas, and condensate with nano-
- 572 confinement effect. Journal of Petroleum Science and Engineering, 193, 107362.
- 573 9. Steefel, C. I., & Hu, M. (2022). Reactive Transport Modeling of Mineral Precipitation and Carbon Trapping
- in Discrete Fracture Networks. Water Resources Research, e2022WR032321.
- 575 10. Asadi, P., & Beckingham, L. E. (2022). Intelligent framework for mineral segmentation and fluid-accessible
- 576 surface area analysis in scanning electron microscopy. Applied Geochemistry, 143, 105387.
- 577 11. Ellis, B., Peters, C., Fitts, J., Bromhal, G., McIntyre, D., Warzinski, R., & Rosenbaum, E. (2011).
- 578 Deterioration of a fractured carbonate caprock exposed to CO2-acidified brine flow. Greenhouse Gases: Science and
- 579 *Technology*, 1(3), 248-260.
- Deng, H., Ellis, B. R., Peters, C. A., Fitts, J. P., Crandall, D., & Bromhal, G. S. (2013). Modifications of
- carbonate fracture hydrodynamic properties by CO2-acidified brine flow. *Energy & Fuels*, 27(8), 4221-4231.
- 582 13. Guo, L., Jiang, Z. xing, & Guo, F. (2015). Mineralogy and fracture development characteristics of marine
- 583 shale-gas reservoirs: A case study of Lower Silurian strata in southeastern margin of Sichuan Basin, China. Journal
- of Central South University.
- 585 14. Tian, X., & Daigle, H. (2019). Preferential mineral-microfracture association in intact and deformed shales
- detected by machine learning object detection. Journal of Natural Gas Science and Engineering.
- 587 15. Ding, W., Li, C., Li, C., Xu, C., Jiu, K., Zeng, W., & Wu, L. (2012). Fracture development in shale and its
- relationship to gas accumulation. Geoscience Frontiers.

- 589 16. Yoon, H., Ingraham, M. D., Grigg, J., Rosandick, B., Mozley, P., Rinehart, A., Mook, W. M., & Dewers, T.
- 590 (2019). Impact of Depositional and Diagenetic Heterogeneity on Multiscale Mechanical Behavior of Mancos Shale,
- New Mexico and Utah, USA. In Memoir 120: Mudstone Diagenesis: Research Perspectives for Shale Hydrocarbon
- Reservoirs, Seals, and Source Rocks.
- 593 17. Gale, J. F. W., Laubach, S. E., Olson, J. E., Eichhubl, P., & Fall, A. (2017). Natural fractures in shale: A
- review and new observations. AAPG Bulletin.
- Na, S. H., Sun, W. C., Ingraham, M. D., & Yoon, H. (2017). Effects of spatial heterogeneity and material
- anisotropy on the fracture pattern and macroscopic effective toughness of Mancos Shale in Brazilian tests. Journal of
- Geophysical Research: Solid Earth. https://doi.org/10.1002/2016JB013374.
- 598 19. Khan, H. J., Spielman-Sun, E., Jew, A. D., Bargar, J., Kovscek, A., & Druhan, J. L. (2021). A critical review
- of the physicochemical impacts of water chemistry on shale in hydraulic fracturing systems. Environmental science
- 600 & technology, 55(3), 1377-1394.
- Bourg, I. C. (2015). Sealing Shales versus Brittle Shales: A Sharp Threshold in the Material Properties and
- Energy Technology Uses of Fine-Grained Sedimentary Rocks. Environmental Science and Technology Letters, 2(10).
- 603 https://doi.org/10.1021/acs.estlett.5b00233
- Li, X., Zhu, H., Zhang, K., Li, Z., Yu, Y., Feng, X., & Wang, Z. (2021). Pore characteristics and pore structure
- deformation evolution of ductile deformed shales in the Wufeng-Longmaxi Formation, southern China. Marine and
- 606 Petroleum Geology, 127, 104992.
- Detwiler, R. L., & Morris, J. P. (2018). Fracture Initiation, Propagation, and Permeability Evolution.
- 608 https://doi.org/10.1002/9781119118657.ch5.
- 609 23. Kuva, J., Siitari-Kauppi, M., Lindberg, A., Aaltonen, I., Turpeinen, T., Myllys, M., & Timonen, J. (2012).
- Microstructure, porosity and mineralogy around fractures in Olkiluoto bedrock. Engineering Geology, 139–140.
- Busch, B., Okamoto, A., Garbev, K., & Hilgers, C. (2021). Experimental fracture sealing in reservoir
- sandstones and its relation to rock texture. Journal of Structural Geology, 153, 104447.
- Brunhoeber, O. M., Anovitz, L. M., Asadi, P., & Beckingham, L. E. (2021). Role of mineralogy in controlling
- fracture formation. ACS Earth and Space Chemistry, 5(11), 3104-3114.

- Spokas, K., Peters, C. A., & Pyrak-Nolte, L. (2018). Influence of Rock Mineralogy on Reactive Fracture
- 616 Evolution in Carbonate-Rich Caprocks. Environmental Science and Technology.
- 617 https://doi.org/10.1021/acs.est.8b01021.
- Salehikhoo, F., & Li, L. (2015). The role of magnesite spatial distribution patterns in determining dissolution
- rates: When do they matter?. Geochimica et Cosmochimica Acta, 155, 107-121.
- 620 28. Atchley, A. L., Navarre-Sitchler, A. K., & Maxwell, R. M. (2014). The effects of physical and geochemical
- heterogeneities on hydro-geochemical transport and effective reaction rates. Journal of contaminant hydrology, 165,
- 622 53-64.
- Wen, H., & Li, L. (2018). An upscaled rate law for mineral dissolution in heterogeneous media: The role of
- time and length scales. Geochimica et Cosmochimica Acta, 235, 1-20.
- 625 30. Beckingham, L. E., Mitnick, E. H., Steefel, C. I., Zhang, S., Voltolini, M., Swift, A. M., ... & Xue, Z. (2016).
- 626 Evaluation of mineral reactive surface area estimates for prediction of reactivity of a multi-mineral sediment.
- 627 Geochimica et Cosmochimica Acta, 188, 310-329.
- 628 31. Oelkers, E. H., Schott, J., Gauthier, J. M., & Herrero-Roncal, T. (2008). An experimental study of the
- dissolution mechanism and rates of muscovite. *Geochimica et Cosmochimica Acta*, 72(20), 4948-4961.
- 630 32. Carroll, S. A., & Walther, J. V. (1990). Kaolinite dissolution at 25 degrees, 60 degrees, and 80 degrees
- 631 C. American Journal of Science, 290(7), 797-810.
- 632 33. Ganor, J., Mogollón, J. L., & Lasaga, A. C. (1995). The effect of pH on kaolinite dissolution rates and on
- activation energy. Geochimica et Cosmochimica Acta, 59(6), 1037-1052.
- 634 34. Gu, X., & Evans, L. J. (2007). Modelling the adsorption of Cd (II), Cu (II), Ni (II), Pb (II), and Zn (II) onto
- fithian illite. Journal of colloid and interface science, 307(2), 317-325.
- Bevan, J., & Savage, D. (1989). The effect of organic acids on the dissolution of K-feldspar under conditions
- relevant to burial diagenesis. Mineralogical Magazine, 53(372), 415-425.
- 638 36. Chen, Y., & Brantley, S. L. (1997). Temperature-and pH-dependence of albite dissolution rate at acid
- 639 pH. Chemical Geology, 135(3-4), 275-290.
- Knauss, K. G., & Wolery, T. J. (1988). The dissolution kinetics of quartz as a function of pH and time at 70
- 641 C. Geochimica et Cosmochimica Acta, 52(1), 43-53.

- Brady, P. V., & Walther, J. V. (1990). Kinetics of quartz dissolution at low temperatures. Chemical
- 643 geology, 82, 253-264.
- Brady, P. V., & Walther, J. V. (1989). Controls on silicate dissolution rates in neutral and basic pH solutions
- at 25 C. Geochimica et Cosmochimica acta, 53(11), 2823-2830.
- 646 40. Palandri, J. L., & Kharaka, Y. K. (2004). A compilation of rate parameters of water-mineral interaction
- kinetics for application to geochemical modeling. Geological Survey Menlo Park CA.
- 648 41. Alkattan, M., Oelkers, E. H., Dandurand, J. L., & Schott, J. (1998). An experimental study of calcite and
- 649 limestone dissolution rates as a function of pH from- 1 to 3 and temperature from 25 to 80 C. Chemical
- 650 *geology*, 151(1-4), 199-214.
- 651 42. Steefel, C. I., Appelo, C. A. J., Arora, B., Jacques, D., Kalbacher, T., Kolditz, O., ... & Yeh, G. T. (2015).
- Reactive transport codes for subsurface environmental simulation. *Computational Geosciences*, 19, 445-478.
- 653 43. Steefel, C. I., & Lichtner, P. C. (1998). Multicomponent reactive transport in discrete fractures: I. Controls
- on reaction front geometry. *Journal of Hydrology*, 209(1-4), 186-199.
- Asadi, P., & Beckingham, L. E. (2021). Integrating Machine/Deep Learning Methods and Filtering
- 656 Techniques for Reliable Mineral Phase Segmentation of 3D X-ray Computed Tomography Images. Energies, 14(15),
- 657 4595.
- 658 45. Bachu, S. (2000). Sequestration of CO2 in geological media: criteria and approach for site selection in
- response to climate change. *Energy conversion and management*, 41(9), 953-970.
- 660 46. Crandell, L. E., Peters, C. A., Um, W., Jones, K. W., & Lindquist, W. B. (2012). Changes in the pore network
- structure of Hanford sediment after reaction with caustic tank wastes. *Journal of contaminant hydrology*, 131(1-4),
- 662 89-99.
- 663 47. Sheng, J., Jiahui, Z. H. A. O., & Ping, Y. U. E. (2022). An Experimental Study of the Effect of CO<sub>2</sub> Water-
- 664 Mancos Shale Interactions on Permeability. International Journal of Earth Sciences Knowledge and
- 665 Applications, 4(1), 26-31.
- Duan, Z., & Sun, R. (2003). An improved model calculating CO2 solubility in pure water and aqueous NaCl
- 667 solutions from 273 to 533 K and from 0 to 2000 bar. Chemical geology, 193(3-4), 257-271.
- Hu, Q., Kalteyer, R., Wang, J., & El-Sobky, H. F. (2019). Nanopetrophysical characterization of the Mancos
- shale formation in the san juan basin of northwestern New Mexico, USA. Interpretation, 7(4), SJ45-SJ65.

- Backeberg, N. R., Iacoviello, F., Rittner, M., Mitchell, T. M., Jones, A. P., Day, R., ... & Striolo, A. (2017).
- Quantifying the anisotropy and tortuosity of permeable pathways in clay-rich mudstones using models based on X-
- 672 ray tomography. Scientific reports, 7(1), 1-12.
- 673 51. Lavrov, A. (2017). Fracture permeability under normal stress: a fully computational approach. Journal of
- Petroleum Exploration and Production Technology, 7(1), 181-194.
- 675 52. Muralidharan, V., Chakravarthy, D., Putra, E., & Schechter, D. S. (2004, June). Investigating fracture
- aperture distributions under various stress conditions using X-ray CT scanner. In PETSOC Canadian International
- Petroleum Conference (pp. PETSOC-2004). PETSOC.
- Ranjith, P. G., & Viete, D. R. (2011). Applicability of the 'cubic law'for non-Darcian fracture flow. Journal
- of Petroleum Science and Engineering, 78(2), 321-327.
- Brown, S. R. (1987). Fluid flow through rock joints: the effect of surface roughness. Journal of Geophysical
- 681 Research: Solid Earth, 92(B2), 1337-1347.
- 55. Zimmerman, R. W., Kumar, S., & Bodvarsson, G. S. (1991, July). Lubrication theory analysis of the
- permeability of rough-walled fractures. In International journal of rock mechanics and mining sciences &
- geomechanics abstracts (Vol. 28, No. 4, pp. 325-331). Pergamon.
- Brunauer, S., Emmett, P. H., & Teller, E. (1938). Adsorption of gases in multimolecular layers. Journal of
- the American chemical society, 60(2), 309-319.
- 687 57. Black, J. R., Carroll, S. A., & Haese, R. R. (2015). Rates of mineral dissolution under CO2 storage
- 688 conditions. Chemical Geology, 399, 134-144.
- 58. Deng, H., Molins, S., Trebotich, D., Steefel, C., & DePaolo, D. (2018). Pore-scale numerical investigation
- of the impacts of surface roughness: Upscaling of reaction rates in rough fractures. Geochimica et Cosmochimica
- 691 Acta, 239, 374-389.
- 59. Zhou, C. X., Hu, R., Li, H. W., Yang, Z., & Chen, Y. F. (2022). Pore-Scale Visualization and Quantification
- of Dissolution in Microfluidic Rough Channels. Water Resources Research, 58(11), e2022WR032255.
- 694 60. Song, W., Ogunbanwo, F., Steinsbø, M., Fernø, M. A., & Kovscek, A. R. (2018). Mechanisms of multiphase
- reactive flow using biogenically calcite-functionalized micromodels. Lab on a Chip, 18(24), 3881-3891.
- 696 61. Zhou, C. X., Hu, R., Deng, H., Ling, B., Yang, Z., & Chen, Y. F. (2023). Surface-Volume Scaling Controlled
- by Dissolution Regimes in a Multiphase Flow Environment. Geophysical Research Letters, 50(18), e2023GL104067.

- 698 62. Jimenez-Martinex, J.; Hyman, J.,D.; Chen, Y.; Carey, J.W.; Porter, M.L.; Kang, Q.; Guthrie Jr., G.;
- Viswanathan, H.S.; Homogenization of Dissolution and Enhanced Precipitation Induced by Bubbles in Multiphase
- 700 Flow Systems. Geophys. Res. Lett. 2020, 47(7), e2020GL087163.